

Received March 2, 2019, accepted March 24, 2019, date of publication March 27, 2019, date of current version April 11, 2019.

Digital Object Identifier 10.1109/ACCESS.2019.2907741

Interoperability Improvement for Wireless Electric Vehicle Charging System Using Adaptive Phase-Control Transmitter

GUANG YANG¹, KAI SONG¹, (Member, IEEE), RUIZHI WEI¹, XIAOHUA HUANG²,
HANG ZHANG¹, QIAN ZHANG³, AND CHUNBO ZHU¹, (Member, IEEE)

¹School of Electrical Engineering and Automation, Harbin Institute of Technology, Harbin 150001, China

²Electrical Engineering and New Material Department, China Electric Power Research Institute, Beijing 100192, China

³State Grid Beijing Power Research Institute, Beijing 102209, China

Corresponding author: Kai Song (kaisong@hit.edu.cn)

This work was supported in part by the Science and Technology Project of State Grid Corporation of China under Grant 52020118000L, in part by the National Natural Science Foundation of China under Grant 51677032 and Grant 51577034, in part by the Natural Science Foundation of Heilongjiang Province under Grant E2017045, and in part by the Harbin Science and Technology Innovation Talents Special Fund Project under Grant 2016RAQXJ002.

ABSTRACT Poor interoperability between the rectangular coil and DD coil leads to significant decline in transmission power and efficiency. This paper proposes an adaptive phase-control transmitter (APCT) which is interoperable with different receiving coils for wireless electric vehicle charging (WEVC). First, an optimized bipolar (BP) coil is designed and APCT is capable of generating different flux distributions for different receiving coils. Second, inverter output currents' detection is used to identify the type of receiving coils. Third, mutual inductance is estimated using the primary-side electrical information. Finally, constant current (CC) charging, as well as efficiency optimization method, is introduced. With an X offset and a Y offset of 50 mm, an experimental setup achieves 3-A CC charging for both rectangular and DD receiving coils. The experimental results agree with the theoretical analysis, demonstrating that the proposed APCT is able to improve interoperability with different types of receiving coils.

INDEX TERMS Interoperability, rectangular coil, DD coil, adaptive phase-control transmitter, mutual inductance estimation.

I. INTRODUCTION

Wireless charging cancels plugging-in cables by transferring energy through a large air gap using magnetic fields [1]–[3]. Nowadays, various wireless electric vehicle charging (WEVC) products have been introduced and it is observed that the advantages of WEVC technology include providing automatic charging, increasing device mobility and reducing battery capacity [2]. However, poor interoperability [4], [5] is the bottleneck for WEVC systems. The issues of interoperability can be addressed from the following aspects:

A. INTEROPERABILITY OF MAGNETIC COUPLERS

Rectangular coil and DD coil are two widely used coil structures [4], [6]. Previous research reveals that the null points of power and efficiency cannot be eliminated when

the rectangular and DD coils are aligned [7]. Thus, WEVC applications using rectangular coils are less compatible with products using DD coils.

To improve poor interoperability of magnetic couplers, a number of methods are proposed. Reference [8] analyzes different output characteristics when square coil and DD coil interoperate. Through the optimization of coil dimension, square coil and DD coil are compatible within a certain range. However, redesigning the coils is difficult in real applications. Reference [9] and [10] compare various known coil structures such as DD, DDQ and bipolar (BP) coils. Then, it is concluded that BP coil can be switched to various excitation modes for different receivers. Furthermore, a self-decoupling method is proposed in [11] to eliminate cross coupling in BP coil and improve system stability. However, the influence of variables such as receiving coil dimension is not analyzed and the changing output current is harmful to EV battery during charging. In [10], DDQ coil keeps the mutual inductance

The associate editor coordinating the review of this manuscript and approving it for publication was Fengjiang Wu.

constant when interoperating with a rectangular coil and a DD coil but the structures are too complicated for simplified WEVC applications. Considering limited space for wireless charger installation, this paper further investigates BP coil based on the analysis shown in [12].

B. INTEROPERABILITY OF COMPENSATION TOPOLOGIES

Due to relatively large leakage inductance, compensation topologies of wireless charging system are needed to minimize the input apparent power and maximize the transfer capability [13]. A few literatures analyze the characteristics of four basic compensation topologies and show limited interoperability. Reference [14] points out that the transfer power and efficiency cannot remain stable when four basic compensation topologies interoperate with each other. Reference [15] reviews the characteristics of four basic compensation topologies. The results show that these topologies are interoperable at some specific loads but the condition is too stringent for real-life applications.

High-order primary-side topologies are proposed to improve interoperability with other topologies. In [16], LCC topology is introduced. Reference [17] presents that the primary coil current is constant when LCC topology is used at primary side. Therefore, the interoperability is improved because the induced voltage at secondary-side is constant for secondary topologies. Reference [18] compares SS and double-sided LCC (DS-LCC) topologies to prove that the DS-LCC topology is less sensitive to variations of self-inductances while the efficiency is higher and steady at lower mutual inductance values, which is suitable for interoperable applications. Common compensation topologies are analyzed and summarized with application examples in [19]. It is concluded that the DS-LCC topology can achieve a load-independent current output, as well as charging control without other converters. For system robustness and simplicity, this paper selects DS-LCC topology for analysis.

This paper proposes an adaptive phase-control transmitter (APCT) using optimized BP coil combined with adaptive output current control method. First, the type of receiving coil is identified by the inverter output current detection. Then, CC charging and efficiency optimization method based on mutual inductance estimation algorithm is introduced. Its improved interoperability with rectangular and DD receiving coils is highlighted. The rest of the sections are organized as follows: Section II presents the structure and theoretical analysis of APCT. Section III gives a detailed investigation of the proposed system and different operating modes. The CC charging control and efficiency optimization method is proposed in Section IV and validated by experiments in Section V. Finally, the conclusions are shown in Section VI.

II. THEORETICAL ANALYSIS OF APCT

A. STRUCTURE OF APCT

The structure of APCT is shown in Fig. 1. Design parameters (coil diameter, number of turns, the distance between

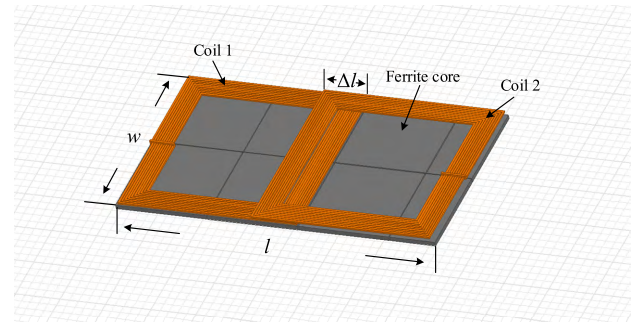


FIGURE 1. Structure of APCT.

each turn, etc.) of two primary coils are identical, as listed in Table 1. The two coils are partially overlapped horizontally to cancel the cross coupling. The flux generated by APCT is altered by controlling the phase difference of two primary currents for the rectangular coil and DD coil, respectively. In addition, the operating frequency is chosen as 85 kHz.

TABLE 1. Design Parameters of APCT.

Symbol	Parameter	Value
l_1 (l_2)	Length of coil 1 (2)	200 mm
l	Length of APCT	350 mm
w	Width of APCT	200 mm
Δl	Overlapping length	50 mm
N_1 (N_2)	Turns of coil 1 (2)	10
t	Distance between each turn	0.5 mm
D	Litz wire diameter	2 mm

As illustrated in [20] and [21], for the multi-transmitter system, when two primary coils are close to each other, the cross coupling between them worsens the power transfer characteristics. To simplify the analysis, a simple mutual inductance model is applied to illustrate the effects of cross coupling on the system from the perspective of reflected impedance, as shown in Fig. 2.

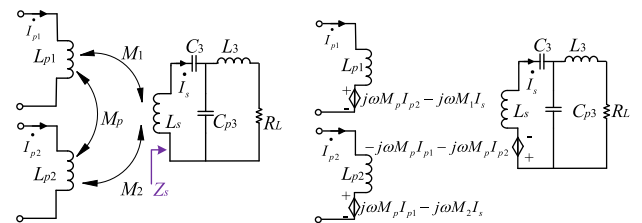
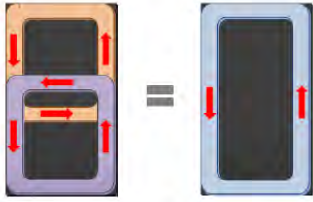
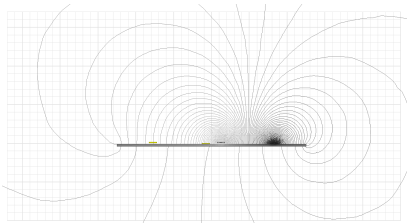
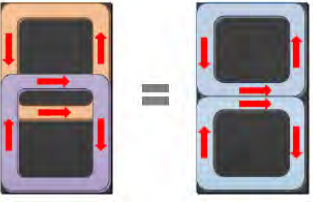
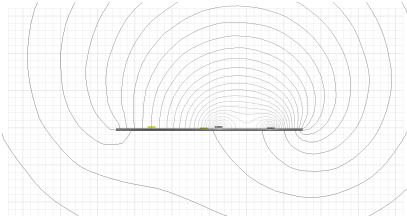


FIGURE 2. Mutual inductance model of APCT. (a) Cross coupling. (b) Decoupled equivalent circuit model.

Assuming that primary currents are in phase and each circuit is completely resonant, according to [20], the reflected impedance from secondary-side to each of the primary-side

TABLE 2. Operating Modes.

Operating mode	Current direction	Flux distribution
SR mode		
DD mode		

is described as (1).

$$\begin{cases} Z_{r1} = \frac{\omega^2 M_1}{Z_s} (M_1 + M_2 \frac{I_{p2}}{I_{p1}}) + j\omega M_p \frac{I_{p2}}{I_{p1}} \\ Z_{r2} = \frac{\omega^2 M_2}{Z_s} (M_2 + M_1 \frac{I_{p1}}{I_{p2}}) + j\omega M_p \frac{I_{p1}}{I_{p2}} \end{cases} \quad (1)$$

where I_{p1} and I_{p2} represent primary currents of two coils, M_1 , M_2 and M_p are mutual inductance between coils, Z_s is the impedance of secondary-side, respectively. According to (1), if cross coupling is not compensated, the imaginary part of Z_{r1} and Z_{r2} exist so that the system becomes detuned because the reflected impedance and original primary-side impedance compensate each other. Moreover, (1) implies that $\text{Im}(Z_{r1})$ and $\text{Im}(Z_{r2})$ are proportional to I_{p1}/I_{p2} . Consequently, the imaginary part of primary-side impedance is not completely compensated when the primary current is changing. In order to improve system robustness, cross coupling should be eliminated.

Based on the analysis in [9], the overlapping area is designed to decouple each other for BP coils. To obtain the appropriate overlapping area, finite element analysis (FEA) and experiments are used for validation. The ratio of overlapping length and the total length is defined as γ :

$$\gamma = \frac{\Delta l}{l} \quad (2)$$

The simulation results and experimental results are shown in Fig. 3. The mutual inductance M_p is used to evaluate cross coupling and higher M_p represents stronger cross coupling. The experimental results show a good coincidence with the simulation results. When γ is selected as 0.17, M_p is close to zero and thus, the cross coupling is canceled. In this way, the structure of APCT is determined.

B. OPERATING MODES

Reference [12] illustrates that the rectangular coil generates vertical flux while the DD coil couples parallel flux polarized

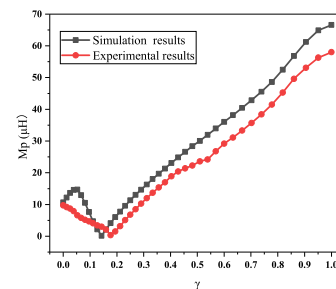


FIGURE 3. Cross coupling versus γ .

along the length of the coil. To ensure the interoperability with various receiving coils, the flux distribution needs to be controlled. As discussed in [9], the proposed coil structure can interoperate with both the rectangular coil and DD coil because of the variable and enhanced magnetic flux generated by APCT. In this paper, single rectangular coil mode (SR mode) and DD coil mode (DD mode) are analyzed in detail as follows.

When primary-side operates in SR mode, APCT generates a vertical magnetic field of which flux density and distribution range are similar to single rectangular coil. Contrary to SR mode, parallel and polarized flux is generated and picked up by DD receiving coil in DD mode. Two typical operating modes are shown in Table 2.

C. COMPARISON OF INTEROPERABILITY BETWEEN COILS

As discussed above, the interoperability can be improved by switching the operating modes. In order to illustrate the effects of operating modes, simulation is performed. A rectangular coil and a DD coil which have the same dimension are adopted as receiving coils. As a reference, transmitters using a rectangular coil and a DD coil are introduced and

the dimension is the same as APCT. The design parameters are shown in Table 3 and 4. To analyze the misalignment between coils, 50 mm offset in both horizontal and vertical direction is considered. In addition, the air gap is 150 mm and 5 mm core thickness is chosen for all the cases in the simulation. Since the two coils in APCT are independent, the total mutual inductance (Coil 1-receiving coil, Coil 2-receiving coil) is defined as the mutual inductance between APCT and the receiving coil.

TABLE 3. Parameters of the Transmitting Coils.

Coil type	Length × width /mm×mm	Number of turns	Self- inductance/μH
Rectangular	350 × 200	12	133
DD	350 × 200	10	152
APCT	350 × 200	10 (Coil 1) 10 (Coil 2)	65 (Coil 1) 65 (Coil 2)

TABLE 4. Parameters of the Receiving Coils.

Coil type	Length × width /mm×mm	Number of turns	Self- inductance/μH
Rectangular	350 × 200	12	132
DD	350 × 200	10	136

Fig. 4 shows the trend of mutual inductance versus offset when different coils interoperate. When a rectangular coil or a DD coil interoperates with the same type coil, the mutual inductance decreases with offset as analyzed in [7], [22]. However, the mutual inductance decreases to zero when a rectangular coil and a DD coil interoperate, as shown in Fig. 4(c) and (d). The phenomenon implies poor interoperability between a rectangular coil and a DD coil. As shown in Fig. 4(e) and (f), when APCT is adopted, the null point of mutual inductance is eliminated and mutual inductance becomes stable if receiving coil changes. Therefore, it is proved that APCT has the potential to interoperate with rectangular coil and DD coil by adjusting the operating modes.

III. CIRCUIT ANALYSIS OF APCT

A. CIRCUIT MODELING

1) SR MODE

Fig. 5(a) shows the circuit model of SR mode. U_{bus} is DC-link voltage. Two independent H-bridge inverters with Buck converter A and B are designed to energize APCT. One DSP controller is utilized to generate two PWM signals with duty cycle D_1 and D_2 for Buck converters, as well as other eight PWM signals to drive the inverters. The mutual inductance between the receiving coil and the two transmitting coils in APCT are defined as M_1, M_2 , respectively. LCC topology is selected to compensate reactive power and achieve constant

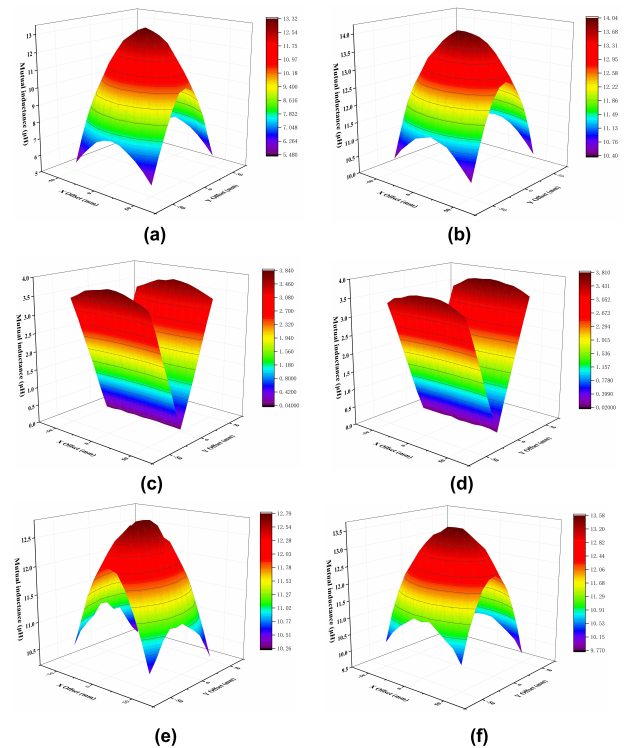


FIGURE 4. Mutual inductance between different coils. (a) Rectangular coil-rectangular coil. (b) DD coil-DD coil. (c) Rectangular coil-DD coil. (d) DD coil-rectangular coil. (e) SR mode-rectangular coil. (f) DD mode-DD coil.

primary current. $L_{p1}, L_{p2}, R_{p1}, R_{p2}$ are self-inductance and equivalent series resistances (ESRs) of primary transmitting coils, L_1, L_2 are compensation inductors of which ESRs are neglected because it is relatively small compared to R_{p1}, R_{p2} . Similar to illustration in [18], the values of resonant capacitors C_{p1}, C_{p2}, C_1, C_2 are designed by (3).

$$\omega = \frac{1}{\sqrt{L_1 C_{p1}}} = \frac{1}{\sqrt{L_2 C_{p2}}} \tag{3}$$

$$\omega = \frac{1}{\sqrt{(L_{p1} - L_1) C_1}} = \frac{1}{\sqrt{(L_{p2} - L_2) C_2}}$$

where ω is operating angular frequency.

To simplify vehicle assembly, only a full-wave rectifier with a capacitive filter is added. The values of secondary resonant capacitors can be obtained:

$$\omega = \frac{1}{\sqrt{L_3 C_{p3}}} \tag{4}$$

$$\omega = \frac{1}{\sqrt{(L_s - L_3) C_3}}$$

To simplify the analysis, the battery is modeled as an equivalent resistor R_L which is related to the battery's state of charge (SOC) [11]. When power losses of the rectifier and filter are ignored, the equivalent load resistor can be reflected

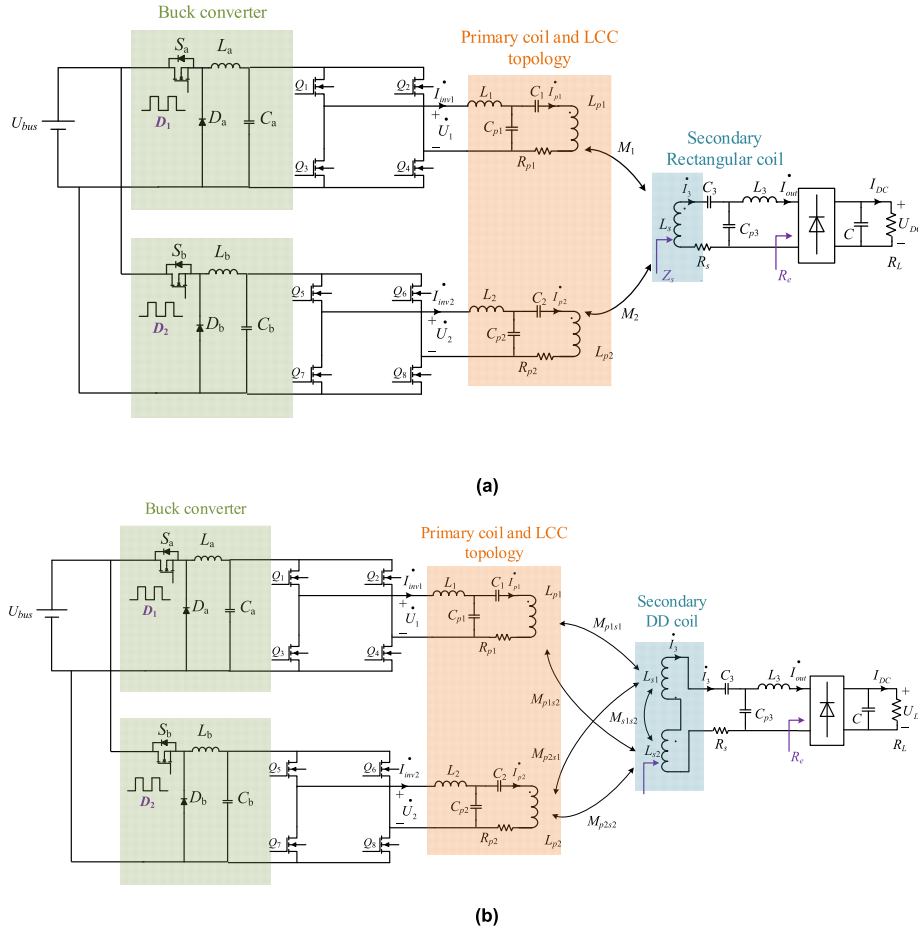


FIGURE 5. Circuit model of APCT. (a) SR mode. (b) DD mode.

to the AC side [23]:

$$R_e = \frac{8}{\pi^2} R_L \quad (5)$$

Further, the impedance of secondary-side at the resonance frequency is derived as:

$$\begin{aligned} Z_s &= j\omega L_s + \frac{1}{j\omega C_3} + R_s + \frac{1}{j\omega C_{p3}} // (j\omega L_3 + R_e) \\ &= R_s + \frac{\pi^2 L_3}{8 R_L C_{p3}} \end{aligned} \quad (6)$$

Design parameters of the primary coils are identical and equation (7) is obtained.

$$\begin{cases} L_{p1} = L_{p2} = L_p \\ L_1 = L_2 = L_0 \\ R_{p1} = R_{p2} = R_p \end{cases} \quad (7)$$

Using Kirchhoff's voltage law (KVL), SR mode can be described by equation (8) based on fundamental harmonic

approximation (FHA) method.

$$\begin{cases} I_1 \cdot (j\omega L_1 + \frac{1}{j\omega C_{p1}}) - I_{p1} \cdot \frac{1}{j\omega C_{p1}} = U_1 \cdot \\ I_{p1} \cdot (j\omega L_{p1} + \frac{1}{j\omega C_{p1}} + \frac{1}{j\omega C_1} + R_{p1}) \\ - I_{inv1} \cdot \frac{1}{j\omega C_{p1}} - j\omega M_1 I_3 \cdot = 0 \\ I_{inv2} \cdot (j\omega L_2 + \frac{1}{j\omega C_{p2}}) - I_{p2} \cdot \frac{1}{j\omega C_{p2}} = U_2 \cdot \\ I_{p2} \cdot (j\omega L_{p2} + \frac{1}{j\omega C_{p2}} + \frac{1}{j\omega C_2} + R_{p2}) \\ - I_{inv2} \cdot \frac{1}{j\omega C_{p2}} - j\omega M_2 I_3 \cdot = 0 \\ -j\omega M_1 I_{p1} \cdot - j\omega M_2 I_{p2} \cdot + I_3 \cdot (j\omega L_s + \frac{1}{j\omega C_{p3}} + \frac{1}{j\omega C_3} + R_s) \\ - I_{out} \cdot \frac{1}{j\omega C_{p3}} = 0 \\ I_{out} \cdot (j\omega L_3 + \frac{1}{j\omega C_{p3}} + R_e) - I_3 \cdot \frac{1}{j\omega C_{p3}} = 0 \end{cases} \quad (8)$$

where the fundamental harmonic of inverter output voltages are sinusoidal and expressed

as:

$$\begin{cases} U_1^* = D_1 U_{bus} \angle 0^\circ = D_1 U_{bus} \\ U_2^* = D_2 U_{bus} \angle \alpha = D_2 U_{bus} (\cos \alpha + j \sin \alpha) \end{cases} \quad (9)$$

In (10), as shown at the top of the next page, α represents the phase difference between U_1 and U_2 . By solving (7)~(9), the output currents of inverters I_{inv1} , I_{inv2} , the primary currents I_{p1} , I_{p2} and equivalent output current I_{out} in SR mode can be derived as:

In general, R_s is relatively small so that (11) is obtained:

$$\omega^2 L_3^2 + R_s R_e \approx \omega^2 L_3^2 \quad (11)$$

Then, the value of I_{out} becomes independent of the load, which proves the constant output current characteristics of DS-LCC topology applied in this paper. Since α is zero or π , the root-mean-square (RMS) value of I_{out} is simplified:

$$\begin{aligned} |I_{out}^*| &= \frac{U_{bus}}{\omega L_0 L_3} \sqrt{(M_1 D_1)^2 + (M_2 D_2)^2 + 2 M_1 M_2 D_1 D_2 \cos \alpha} \end{aligned} \quad (12)$$

For SR mode, it is obvious that M_1 and M_2 are greater than zero, as shown in Fig. 6. From equation (12), RMS value of I_{out} reaches maximum if α equals to zero and minimum if α is chosen as π . To improve output power, α needs to be adjusted to zero when SR mode is activated.

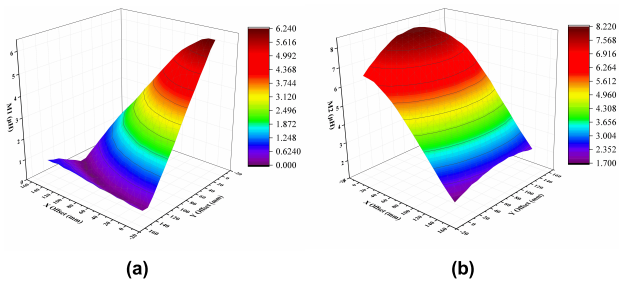


FIGURE 6. M_1 and M_2 versus offset. (a) M_1 . (b) M_2 .

2) DD MODE

As presented in [24], the winding of the DD coil is such that one D coil is instantaneously a north pole and the other is a south pole. Hence, the DD coil is equivalent to two reversely series connected rectangular coils, as shown in Fig. 5(b). When the DD coil is decomposed by this method, the coupling condition becomes complicated. M_{p1s1} , M_{p1s2} , M_{p2s1} , M_{p2s2} and M_{s1s2} are mutual inductance between coils, where M_{s1s2} is constant and measurable once the DD coil structure is fixed.

Then, DD mode is described as (13), as shown at the top of the next page. M_{s1s2} needs to be compensated so that the secondary-side series capacitor C_3 is obtained:

$$\omega = \frac{1}{\sqrt{(L_{s1} + L_{s2} - 2M_{s1s2} - L_3)C_3}} \quad (14)$$

To simplify equation (13), the followings are assumed:

$$\begin{cases} M'_1 = M_{p1s1} - M_{p1s2} \\ M'_2 = M_{p2s1} - M_{p2s2} \end{cases} \quad (15)$$

Substituting (15) into (13) gives (16), as shown at the top of the next page:

$$\begin{aligned} |I_{out}^*| &= \frac{U_{bus}}{\omega L_0 L_3} \sqrt{(M'_1 D_1)^2 + (M'_2 D_2)^2 + 2 M'_1 M'_2 D_1 D_2 \cos \alpha} \end{aligned} \quad (17)$$

Comparing (13) and (17), it is shown that DD mode has similar output characteristics as SR mode. However, for DD mode, it is uncertain whether M'_1 and M'_2 are greater or less than zero at different offsets. Fig. 7 shows M'_1 and M'_2 versus offset. It is clear that $(M'_1 M'_2)$ is smaller than zero at almost all offsets. Combined with (17), for maximum I_{out} , α needs to be π . An adaptive phase control method will be detailed in Section IV-A.

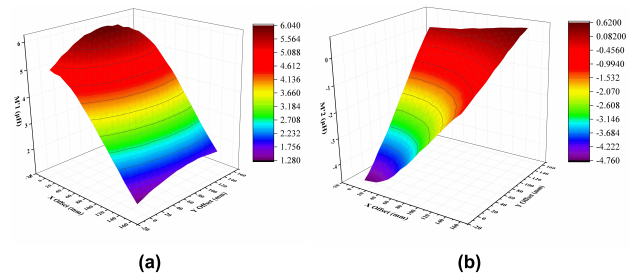


FIGURE 7. M'_1 and M'_2 versus offset. (a) M'_1 . (b) M'_2 .

B. OUTPUT CURRENT CHARACTERISTICS

Since DS-LCC topology is used, the output current is only related to primary voltage and mutual inductance when the circuit parameters are fixed [18]. The circuit parameters are listed in Table 5. As illustrated in [11] and [23], only active power is considered when studying the output power and transmission efficiency below. The transmission efficiency in this paper is AC-DC efficiency which is from inverter output to load.

TABLE 5. Circuit Parameters of the System.

Symbol	Parameter	Value	Unit
U_{bus}	Input DC voltage	48	V
L_1 (L_2)	Primary-side series inductor	14	μH
C_{p1} (C_{p2})	Primary-side parallel capacitor	250	nF
C_1 (C_2)	Primary-side series capacitor	66	nF
R_{p1} (R_{p2})	Primary coil resistance	0.04	Ω
R_s	Secondary coil resistance	0.04	Ω
C_3	Secondary-side series capacitor	27	nF
C_{p3}	Secondary-side parallel capacitor	473	nF
L_3	Secondary-side series inductor	7.4	μH
R_L	Load resistor	5	Ω

$$\begin{cases} I_{inv1}^{\bullet} = \frac{\omega^2 M_1^2 D_1 U_{bus} + R_p(\omega^2 L_3 + R_s R_e) D_1 U_{bus} + \omega^2 M_1 M_2 D_2 U_{bus}(\cos \alpha + j \sin \alpha)}{\omega^2 L_0 L_3 (\omega^2 L_3 + R_s R_e)} \\ I_{inv2}^{\bullet} = \frac{\omega^2 M_1 M_2 D_1 U_{bus} + [\omega^2 M_2^2 + R_p(\omega^2 L_3 + R_s R_e)] D_2 U_{bus}(\cos \alpha + j \sin \alpha)}{\omega^2 L_0 L_3 (\omega^2 L_3 + R_s R_e)} \\ I_{p1}^{\bullet} = j \left(\frac{-D_1 U_{bus}}{\omega L_0} \right) \\ I_{p2}^{\bullet} = \frac{D_2 U_{bus}}{\omega L_0} (\sin \alpha - j \cos \alpha) \\ I_{out}^{\bullet} = \frac{\omega L_3}{L_0 (\omega^2 L_3^2 + R_s R_e)} [j M_1 D_1 + (j \cos \alpha - \sin \alpha) M_2 D_2] U_{bus} \end{cases} \quad (10)$$

$$\begin{cases} I_{inv1}^{\bullet} (j\omega L_1 + \frac{1}{j\omega C_{p1}}) - I_{p1}^{\bullet} \cdot \frac{1}{j\omega C_{p1}} = U_1^{\bullet} \\ I_{p1}^{\bullet} (j\omega L_{p1} + \frac{1}{j\omega C_{p1}} + \frac{1}{j\omega C_1} + R_{p1}) - I_{inv1}^{\bullet} \cdot \frac{1}{j\omega C_{p1}} + j\omega M_{p1s1} I_3^{\bullet} - j\omega M_{p1s2} I_3^{\bullet} = 0 \\ I_{inv2}^{\bullet} (j\omega L_2 + \frac{1}{j\omega C_{p2}}) - I_{p2}^{\bullet} \cdot \frac{1}{j\omega C_{p2}} = U_2^{\bullet} \\ I_{p2}^{\bullet} (j\omega L_{p2} + \frac{1}{j\omega C_{p2}} + \frac{1}{j\omega C_2} + R_{p2}) - I_{inv2}^{\bullet} \cdot \frac{1}{j\omega C_{p2}} + j\omega M_{p2s1} I_3^{\bullet} - j\omega M_{p2s2} I_3^{\bullet} = 0 \\ j\omega M_{p1s1} I_{p1}^{\bullet} - j\omega M_{p1s2} I_{p1}^{\bullet} + j\omega M_{p2s1} I_{p2}^{\bullet} - j\omega M_{p2s2} I_{p2}^{\bullet} + I_3^{\bullet} (j\omega L_{s1} + j\omega L_{s2} - 2j\omega M_{s1s2} + \frac{1}{j\omega C_{p3}} + \frac{1}{j\omega C_3} + R_s) \\ \quad - I_{out}^{\bullet} \cdot \frac{1}{j\omega C_{p3}} = 0 \\ I_{out}^{\bullet} (j\omega L_2 + \frac{1}{j\omega C_{p2}} + R_e) - I_3^{\bullet} \cdot \frac{1}{j\omega C_{p3}} = 0 \end{cases} \quad (13)$$

$$\begin{cases} I_{inv1}^{\bullet} = \frac{\omega^2 M_1^2 D_1 U_{bus} + R_p(\omega^2 L_3 + R_s R_e) D_1 U_{bus} + \omega^2 M_1' M_2' D_2 U_{bus}(\cos \alpha + j \sin \alpha)}{\omega^2 L_0 L_3 (\omega^2 L_3 + R_s R_e)} \\ I_{inv2}^{\bullet} = \frac{\omega^2 M_1' M_2' D_1 U_{bus} + [\omega^2 M_2'^2 + R_p(\omega^2 L_3 + R_s R_e)] D_2 U_{bus}(\cos \alpha + j \sin \alpha)}{\omega^2 L_0 L_3 (\omega^2 L_3 + R_s R_e)} \\ I_{p1}^{\bullet} = j \left(\frac{-D_1 U_{bus}}{\omega L_0} \right) \\ I_{p2}^{\bullet} = \frac{D_2 U_{bus}}{\omega L_0} (\sin \alpha - j \cos \alpha) \\ I_{out}^{\bullet} = \frac{\omega L_3}{L_0 (\omega^2 L_3^2 + R_s R_e)} [j M_1' D_1 + (j \cos \alpha - \sin \alpha) M_2' D_2] U_{bus} \end{cases} \quad (16)$$

1) SR MODE

Generally, Buck converter can be used to control output current I_{out} by adjusting the duty cycle of the driving signal. In SR mode, the influence of primary Buck converters on output current is shown in Fig. 8. In practice, the duty cycle of the driving signal of Buck converter is regulated from 0.2 to 0.8 for system stability [23]. Typical duty cycle values are chosen and the corresponding I_{out} is plotted. It is shown that I_{out} increases linearly with the increase of D_1 and D_2 . Aiming at 3 A CC charging, it is obvious that I_{out} can be regulated to 3 A with or without misalignment.

2) DD MODE

As discussed before, DD mode is also analyzed based on the above principle. It is clear that the curves are similar to those

in SR mode. 3 A is also set as target value of I_{out} . The same CC charging control principle is applied.

C. EFFICIENCY OPTIMIZATION

1) SR MODE

As illustrated In Section III-B, CC charging can be achieved by adjusting the values of D_1 and D_2 for different receivers. However, it is hard to determine the accurate values of D_1 and D_2 since the proposed system is energized by two independent inverters and the power allocation influences the transmission efficiency. To achieve high efficiency, the optimized output current control method is introduced as follows.

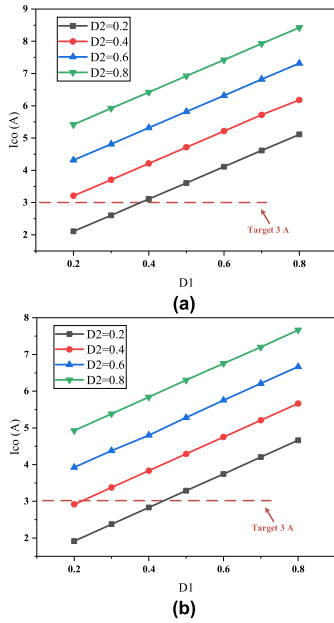


FIGURE 8. Output current versus different D_1 and D_2 (SR mode). (a) X offset = 0 mm, Y offset = 0 mm. (b) X offset = 50 mm, Y offset = 50 mm.

According to (13), since α is set as zero, the input power P_{in-CR} is calculated as:

$$\begin{aligned}
 P_{in-CR} &= U_1 I_1 + U_2 I_2 \\
 &= \frac{(M_1^2 + R_p L_3) D_1^2 + 2 M_1 M_2 D_1 D_2 + (M_2^2 + R_p L_3) D_2^2}{\omega^2 L_3^2 L_0} U_{bus}^2
 \end{aligned} \tag{18}$$

To simplify the analysis, power losses of the rectifier and the filter are ignored. Then, the output power P_{out-CR} is expressed as:

$$\begin{aligned}
 P_{out-CR} &= I_{out}^2 R_e \\
 &= \frac{(M_1 D_1)^2 + (M_2 D_2)^2 + 2 M_1 D_1 M_2 D_2}{(\omega L_0 L_3)^2} U_{bus}^2 R_e
 \end{aligned} \tag{19}$$

Assuming the ratio of U_1 and U_2 is (20), as shown at the bottom of the next page.

The transmission efficiency, η_{CR} can be derived as (21), as shown at the bottom of the next page. It is shown that η_{CR} is the function of λ . To calculate the optimal λ for maximum efficiency, the first and the second derivative of η_{CR} against λ are derived.

$$\begin{cases} \frac{\partial \eta_{CR}}{\partial \lambda} = 0 \\ \frac{\partial^2 \eta_{CR}}{\partial \lambda^2} < 0 \end{cases} \tag{22}$$

Solving (22) gives:

$$\lambda_{opt} = \frac{M_1}{M_2} \tag{23}$$

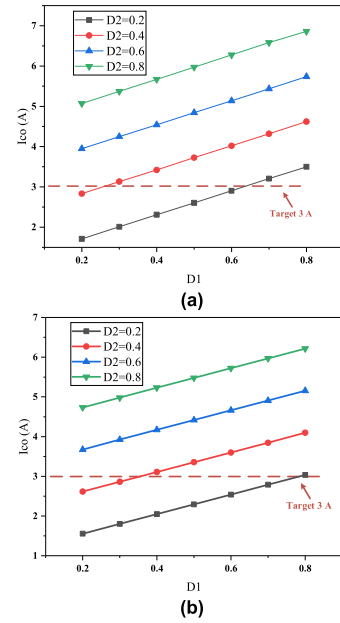


FIGURE 9. Output current versus different D_1 and D_2 (DD mode). (a) X offset = 0 mm, Y offset = 0 mm. (b) X offset = 50 mm, Y offset = 50 mm.

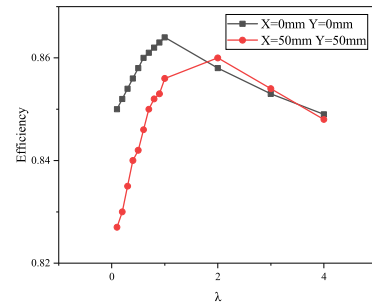


FIGURE 10. Transmission efficiency versus λ (SR mode, $D_2 = 0.2$).

As indicated in (23), the transmission efficiency reaches a maximum when the ratio λ is set as λ_{opt} . When λ is set to λ_{opt} , the ratio of D_1 and D_2 is expressed as:

$$\lambda_{opt} = \frac{D_1}{D_2} \tag{24}$$

(21) shows that the transmission efficiency is related to λ instead of D_1 and D_2 . Assuming that D_2 equals 0.2, the trend of the transmission efficiency versus λ is plotted in Fig. 10. When the transmitter and the receiving coil are aligned, λ_{opt} equals 1 and the transmission efficiency reaches the maximum at $\lambda = 1$. When coils are misaligned, 50 mm offset is taken as an example. From Fig. 6, λ_{opt} is about 2 when X and Y offset are 50 mm, which shows agreement with the above theoretical analysis. Briefly, by adjusting λ to λ_{opt} , the maximum transmission efficiency can be achieved.

By solving (13) and (24), the duty cycle to ensure constant output current and maximum efficiency are calculated:

$$\begin{cases} D_{1-opt} = \frac{I_{co} L_0 (\omega^2 L_3 + R_s R_e) M_1}{2 U_{bus} \omega L_3 (M_1^2 + M_2^2)} \\ D_{2-opt} = \frac{I_{co} L_0 (\omega^2 L_3 + R_s R_e) M_2}{2 U_{bus} \omega L_3 (M_1^2 + M_2^2)} \end{cases} \tag{25}$$

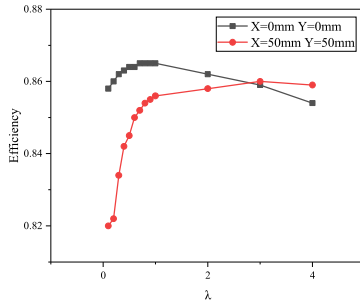


FIGURE 11. Transmission efficiency versus λ (DD mode, D₂ = 0.2).

According to (25), D_1 and D_2 can be calculated when M_1 and M_2 are known so that CC charging is realized and the transmission efficiency is optimized. The method to estimate M_1 and M_2 by primary-side electrical information will be introduced in Section IV.

2) DD MODE

Transmission efficiency in DD mode has the same characteristics as that in SR mode, as shown in Fig. 11.

The corresponding D_1 and D_2 can be calculated:

$$\begin{cases} D_{1-opt} = \frac{I_{co}L_0(\omega^2L_3 + R_sR_e) |M'_1|}{2U_{bus}\omega L_3(M_1'^2 + M_2'^2)} \\ D_{2-opt} = \frac{I_{co}L_0(\omega^2L_3 + R_sR_e) |M'_2|}{2U_{bus}\omega L_3(M_1'^2 + M_2'^2)} \end{cases} \quad (26)$$

Equation (26) shows a similar conclusion as SR mode, which implies that the same control principle can also be applied in DD mode.

In conclusion, whether working in SR mode or DD mode, the duty cycle can be determined by the proposed method according to (25) and (26). Then, CC charging and efficiency optimization can be realized. Mutual inductance estimation algorithm and other control strategies will be detailed in Section IV.

IV. CONTROL STRATEGY OF APCT

The control scheme of the system is shown in Fig. 12 and the control strategy is detailed below.

A. RECEIVING COIL IDENTIFICATION AND ADAPTIVE OPERATING MODE SWITCHING CONTROL

The type of the receiving coil should be detected so that the operating mode can be determined. The detection

using wireless communication has been studied in previous research. Without wireless communication, this paper proposes a novel detection method using inverter output current. In this paper, inverter output currents are compared when different operating modes are motivated. The comparison results can distinguish the type of receiving coil and then determine the operating mode.

1) IF THE RECEIVING COIL IS RECTANGULAR COIL

From (11), when receiving coil is rectangular coil, inverter output current I_{inv1} and I_{inv2} can be simplified:

$$\begin{cases} I_{inv1}|_{\alpha=0} = \frac{[\omega^2M_1^2D_1 + \omega^2R_pL_3D_1 + \omega^2M_1M_2D_2]U_{bus}}{\omega^4L_3^2L_0} \\ I_{inv1}|_{\alpha=\pi} = \frac{[\omega^2M_1^2D_1 + \omega^2R_pL_3D_1 - \omega^2M_1M_2D_2]U_{bus}}{\omega^4L_3^2L_0} \end{cases} \quad (27)$$

$$\begin{cases} I_{inv2}|_{\alpha=0} = \frac{[\omega^2M_1M_2D_1 + (\omega^2M_2^2 + \omega^2R_pL_3)D_2]U_{bus}}{\omega^4L_3^2L_0} \\ I_{inv2}|_{\alpha=\pi} = \frac{[\omega^2M_1M_2D_1 - (\omega^2M_2^2 + \omega^2R_pL_3)D_2]U_{bus}}{\omega^4L_3^2L_0} \end{cases} \quad (28)$$

It is obvious that

$$\begin{cases} I_{inv1}|_{\alpha=0} > I_{inv1}|_{\alpha=\pi} \\ I_{inv2}|_{\alpha=0} > I_{inv2}|_{\alpha=\pi} \end{cases} \quad M_1M_2 > 0 \quad (29)$$

For rectangular receiving coil, I_{inv1} and I_{inv2} in SR mode are higher than those in DD mode. Thus, I_{inv1} and I_{inv2} can be compared in different operating modes to decide the appropriate one.

2) IF THE RECEIVING COIL IS DD COIL

Combined with (16), when receiving coil is DD coil, the relationship of I_{inv1} and I_{inv2} is related to M'_1 and M'_2 :

$$\begin{cases} I_{inv1}|_{\alpha=0} < I_{inv1}|_{\alpha=\pi} \\ I_{inv2}|_{\alpha=0} < I_{inv2}|_{\alpha=\pi} \end{cases} \quad M'_1M'_2 < 0 \quad (30)$$

For DD receiving coil, I_{inv1} and I_{inv2} in DD mode are higher.

For the unknown-type receiving coil, the workflow of the proposed method is shown in Fig. 13. The initial selection is

$$\lambda = \frac{U_1}{U_2} = \frac{D_1}{D_2} \quad (20)$$

$$\eta_{CR} = \frac{P_{out-CR}}{P_{in-CR}} \quad (21)$$

$$= \frac{\omega^6L_3^4(\lambda M_1 + M_2)^2R_e}{L_0(\omega^2L_3^2)^2\{\lambda^2\omega^2M_1^2 + 2\lambda\omega^6L_0L_3^2M_1M_2 + \omega^2L_3^2[\lambda^2R_p + \omega^2L_0L_3(M_2^2 + L_3R_p)]\}}$$

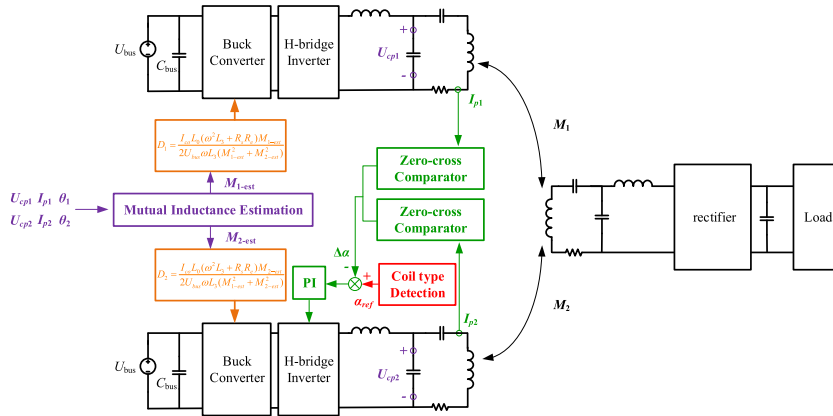


FIGURE 12. The control scheme of the proposed system.

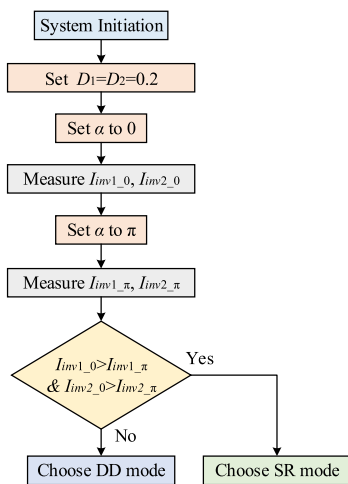


FIGURE 13. Flowchart of operating mode switching.

independent of vehicle location or coil parameters, which is much easier to accomplish.

Control of α needs to be accurate. In practice, the parameters of passive components in the compensation network are not completely identical. Besides, the temperature drift of the components also occurs during the charging process. Considering the component errors and temperature drift, robust control of the phase difference is shown in Fig. 12. α_{ref} is determined by initial selection according to receiving coil type. Then, using PI algorithm, the driving signal of inverter A is unchanged while the driving signal of inverter B is adjusted with a real-time phase difference of I_{p1} and I_{p2} .

B. MUTUAL INDUCTANCE ESTIMATION USING PRIMARY-SIDE ELECTRICAL INFORMATION

As analyzed in Section III, accurate mutual inductance estimation is essential to system control. Reference [25] proposes a simultaneous estimation method of the primary voltage and the mutual inductance using only secondary-side information. However, the method is not suitable for multi-transmitter

systems because individual mutual inductance cannot be recognized. Therefore, primary-side electrical information such as inverter output voltage and current are used to calculate mutual inductance based on SS topology in [26], [27], as well as LCL-P topology in [28]. However, for DS-LCC topology, the distorted current waveform which seriously reduces estimation accuracy at low mutual inductance is not studied.

Taking M_1 as an example, the reflected impedance from the secondary-side to primary-side can be expressed as:

$$Z_{r1} = \frac{(\omega M_1)^2}{Z_s} = \frac{8(\omega M_1)^2 R_L C_{p3}}{8R_L R_s C_{p3} + \pi^2 L_3} \quad (31)$$

In (31), the effect of a full-wave rectifier with a capacitive filter is considered. Then, it is easy to obtain the output active power of the two inverters:

$$P_1 = I_{p1}^2 (Z_{r1} + R_{p1}) = I_{p1}^2 \left(\frac{8(\omega M_1)^2 R_L C_{p3}}{8R_L R_s C_{p3} + \pi^2 L_3} + R_{p1} \right) \quad (32)$$

In practice, ESRs of coils, compensation inductors and capacitors are known. The value of R_L can be obtained via wireless communication. Therefore, the mutual inductance M_1 can be expressed as:

$$M_1 = \frac{1}{\omega} \sqrt{\frac{(P_1 - I_{p1}^2 R_{p1})(\pi^2 L_3 + 8C_{p3} R_L R_s)}{8C_{p3} R_L I_{p1}^2}} \quad (33)$$

In general, P_1 can be calculated with the inverter output voltage and current [26], [28]. However, since DS-LCC topology is applied, input high-order harmonics make the inverter output current waveform distorted. Fig. 14 shows the inverter output voltage and current simulation waveform of the proposed system. It is hard to measure the phase difference between the voltage and current accurately because of the irregular current waveform. Thus, P_1 is difficult to obtain accurately.

To avoid the above drawbacks, in this paper, the voltage of the parallel capacitor U_{Cp1} is introduced to calculate P_1 , as shown in Fig. 15.

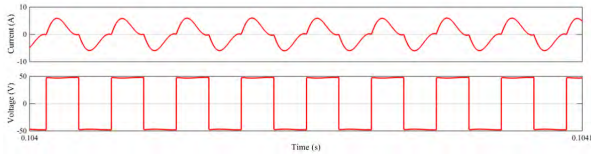


FIGURE 14. Inverter output voltage and current using DS-LCC topology.

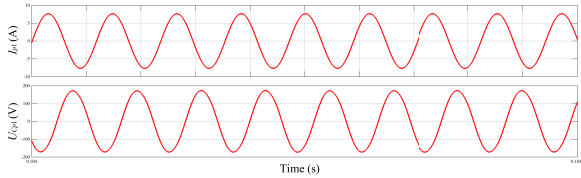


FIGURE 15. Primary coil current and parallel capacitor voltage.

Assuming that

$$Z_{p1} = j\omega L_{p1} + \frac{1}{j\omega C_1} \quad (34)$$

U_{Cp1} is deduced as:

$$\begin{aligned} U_{Cp1} \bullet &= I_{p1} \bullet (j\omega L_{p1} + \frac{1}{j\omega C_1} + Z_{r1} + R_{p1}) \\ &= I_{p1} \bullet (Z_{p1} + Z_{r1} + R_{p1}) \end{aligned} \quad (35)$$

Then, the output apparent power of the inverter is:

$$S_1 = U_{Cp1} I_{p1} = I_{p1}^2 Z_{p1} + I_{p1}^2 (Z_{r1} + R_{p1}) = Q_1 + P_1 \quad (36)$$

where Q_1 is output reactive power. P_1 can be further expressed as:

$$P_1 = S_1 \cos \theta_1 = U_{Cp1} I_{p1} \cos \theta_1 \quad (37)$$

where θ_1 is the phase difference between U_{Cp1} and I_{p1} .

θ_1 can be measured because the waveforms are sinusoidal. Fig. 16 presents the estimation results using the above two methods in simulation. M_{est} is the mutual inductance estimated and M_{ref} is the reference value in the simulation. It is clear that the proposed method is more accurate. The error using the conventional method is higher due to the input harmonics.

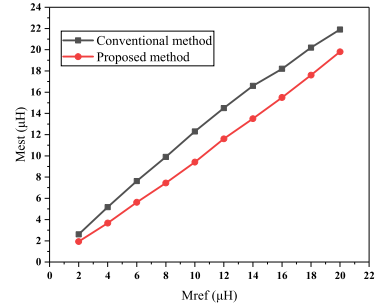
C. CC CHARGING CONTROL

The principle of CC charging control is shown in Fig. 12. After the mutual inductance is estimated, DSP controller adjusts the duty cycle of the Buck converters' driving signal to D_{1_opt} and D_{2_opt} , the output current is controlled and the maximum transmission efficiency is tracked.

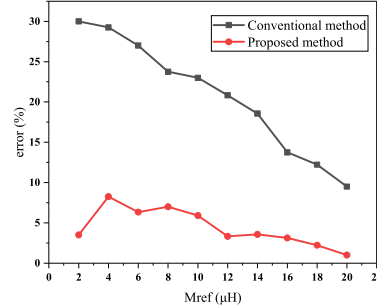
V. EXPERIMENTAL VALIDATION

A. EXPERIMENTAL SETUP

An experimental system shown in Fig. 17 is built to verify the proposed method. The design parameters of coils are the same as that listed in Table 1. H-bridge inverter A and B



(a)



(b)

FIGURE 16. Simulation results of mutual inductance estimation. (a) Estimation results. (b) Relative error.

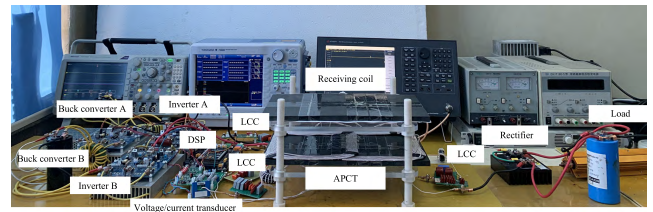


FIGURE 17. Experimental setup.

adopt the same MOSFETs Infineon IPW60R041C6, as well as other circuit components. For the compensation circuit, the circuit parameters are listed in Table 5. The rectifier using diodes IXYS DSEI2x101-12A and capacitive filter supply DC voltage to the load.

DSP TMS320F28335 is adopted as the controller. The current transducer LEM LA55-P and additional high-frequency voltage measurement circuit are applied to measure primary current and parallel capacitor voltage for mutual inductance estimation, respectively. DSP controller generates four phase-controllable PWM signals to the inverter A, B and two PWM signals with appropriate duty cycle to the Buck converter A, B. The waveforms are recorded by the oscilloscope Agilent DSO-X3034A, and the transmission efficiency is measured by the power analyzer Yokogawa PX8000.

B. IDENTIFICATION OF RECEIVING COIL TYPE

To identify the receiving coil type, the operating mode is switched and inverter output currents are measured with rectangular coil and DD coil, respectively. The results are shown as below:

1) IF THE RECEIVING COIL IS RECTANGULAR COIL

Set D_1 and D_2 to 0.2, the inverter output voltage is 8 V. The waveforms of inverter output current I_{inv1} and I_{inv2} are shown in Fig. 18. The red waveform is I_{inv1} while the green one shows I_{inv2} . For rectangular coil, I_{inv1} and I_{inv2} in SR mode are much higher than those in DD mode, which agrees with the above theoretical analysis.

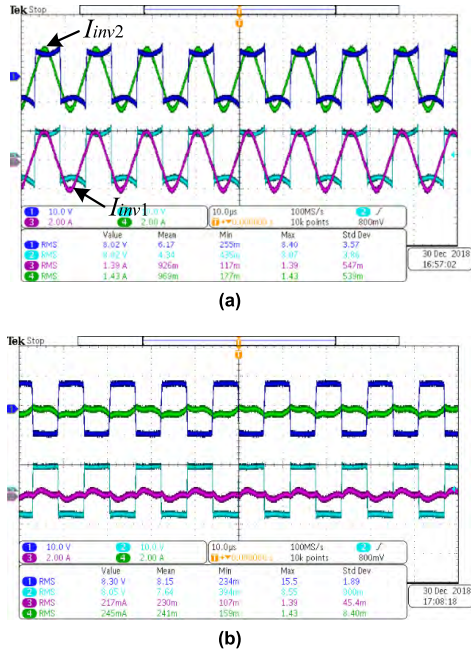


FIGURE 18. Waveforms of I_{inv1} and I_{inv2} (rectangular coil, $D_1 = D_2 = 0.2$). (a) SR mode. (b) DD mode.

2) IF THE RECEIVING COIL IS DD COIL

Fig.19 shows the waveforms of I_{inv1} and I_{inv2} when receiving coil is DD coil. Contrary to rectangular coil, when DD coil is used as receiving coil, I_{inv1} and I_{inv2} are higher if DD mode is activated.

In conclusion, for unchanged input voltage, obvious change of inverter output currents in different operating modes is proved. Therefore, receiving coil type can be identified by comparing inverter output currents.

C. ESTIMATION OF MUTUAL INDUCTANCE

To validate the proposed inductance estimation method, the coil location is changed and some values of mutual inductance are measured as reference. The measured values M_{ref} , estimated values M_{est} , errors and electrical parameters needed for estimation are listed in Table 6.

The maximum estimation error shown in Table 6 is greater than simulation results. The main causes are listed as follows:

- i) In the simulation, circuit components are replaced by ideal models and the mutual inductance calculation is based on FHA method. However, the internal resistance of capacitors cannot be neglected in experiments. Thus, the internal resistance and detuning make the error increase.

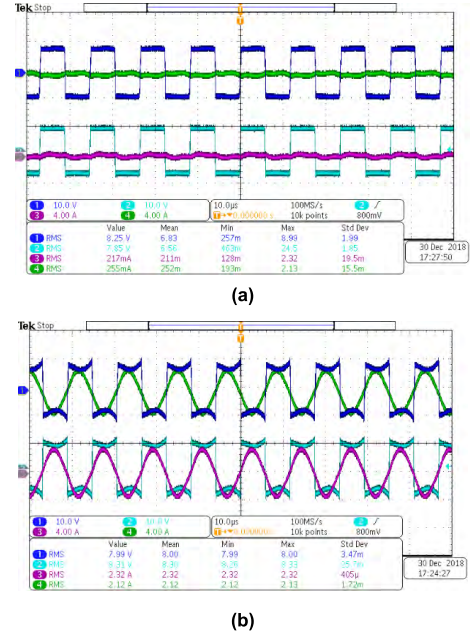


FIGURE 19. Waveforms of I_{inv1} and I_{inv2} (DD coil, $D_1 = D_2 = 0.2$). (a) SR mode. (b) DD mode.

TABLE 6. Inductance Estimation Results.

$M_{ref}/\mu\text{H}$	$U_{Cp1-RMS}/\text{V}$	I_{p1-RMS}/A	θ_1	$M_{est}/\mu\text{H}$	errors
12.0	32.2	1.4	72.36°	13.1	10.7%
6.8	22.8	1.2	67.11°	8.4	23%
$M_{ref}/\mu\text{H}$	$U_{Cp2-RMS}/\text{V}$	I_{p2-RMS}/A	θ_2	$M_{est}/\mu\text{H}$	errors
12.6	33.1	1.2	46.62°	14.3	13%
12.1	30.8	1.1	65.76°	11.3	6.6%

ii) The phase difference of 85 kHz voltage signal is hard to detect accurately due to the limitation of sampling rate. Therefore, this paper adopts the high frequency voltage measurement circuit instead of individual Hall voltage sensor to improve measurement accuracy but still causes an error to the measured value of θ .

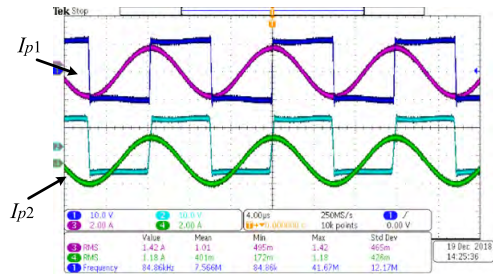
iii) Poor consistency and temperature drift of capacitors also reduce estimation accuracy.

D. INTEROPERABILITY VALIDATION—CC CHARGING AND EFFICIENCY OPTIMIZATION

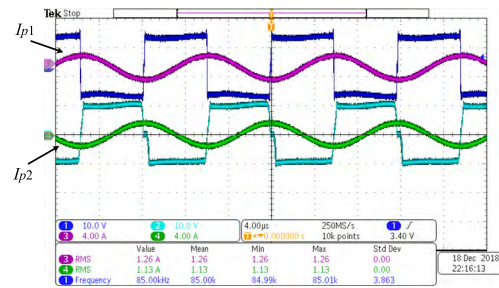
1) DIFFERENT RECEIVING COILS

In order to verify the interoperability improvement using APCT, an experiment on charging DC current I_{DC} and transmission efficiency is performed. With rectangular receiving coil, in-phase primary currents I_{p1} , I_{p2} are shown in Fig. 20(a). Then, α is adjusted and the I_{DC} is measured, as shown in Fig.21.

I_{DC} and efficiency are measured with different duty cycles D_1 and D_2 , as shown in Table 7. The experimental results show that the 3 A CC charging can be achieved and efficiency reaches maximum 74.2% when λ equals 0.97. The measured efficiency and λ are lower than calculated one because internal



(a)



(b)

FIGURE 20. Primary coil current waveforms.(a) SR mode. (b) DD mode.

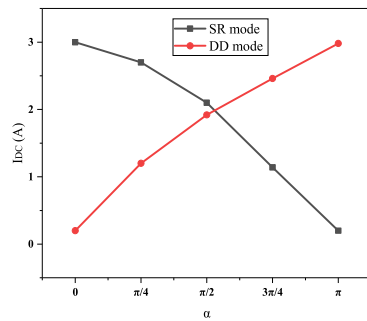


FIGURE 21. I_{DC} vs. α .

TABLE 7. of Different Duty Cycles (SR Mode, Aligned).

D_1	D_2	λ	I_{DC} / A	efficiency
0.1	0.59	0.16	2.99	73.2%
0.2	0.47	0.42	2.99	73.8%
0.33	0.34	0.97	2.99	74.2%
0.54	0.1	5.4	3.0	73.6%

TABLE 8. Comparison of Different Duty Cycles (DD Mode, Aligned).

D_1	D_2	λ	I_{DC} / A	efficiency
0.1	0.42	0.23	2.99	70.8%
0.26	0.25	1.04	2.99	71.3%
0.41	0.12	3.33	2.99	71.0%

resistance of components is not calculated and primary coils are not perfectly symmetric.

With DD receiving coil, I_{p1} and I_{p2} that are out of phase are shown in Fig. 20(b). The curve of I_{DC} versus α is also shown

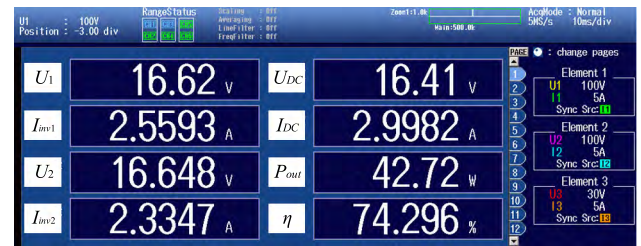


FIGURE 22. System performance of SR mode (aligned).



FIGURE 23. System performance of DD mode (aligned).

TABLE 9. Comparison of Different Duty Cycles (SR Mode, X Offset= 50 mm, Y Offset= 50 mm).

D_1	D_2	λ	I_{DC} / A	efficiency
0.12	0.87	0.13	2.99	75.8%
0.35	0.35	1	2.99	76.8%
0.43	0.22	1.95	2.99	77.3%
0.47	0.11	4.27	2.99	77.0%

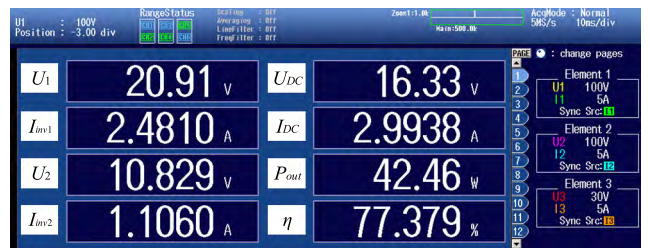


FIGURE 24. System performance with misalignment.

in Fig. 21 and it is clear that the optimal α is π . The influence of D_1 and D_2 is listed in Table 8 and the experimental results of DD mode are shown in Fig. 23. For rectangular coil and DD coil, I_{DC} can be constant and efficiency is optimized using APCT so that the interoperability is improved.

2) INFLUENCE OF MISALIGNMENT

Above experiments prove that APCT is interoperable with rectangular and DD coils, simultaneously. Then, influence of misalignment is verified taking SR mode as an example. When X and Y offset reach 50 mm, λ is calculated as 2. I_{DC} and efficiency versus D_1 , D_2 are listed in Table 9 and Fig. 24. Compared with Table 7, the transmission efficiency is higher because the load may be closer to the optimal one.

VI. CONCLUSION

This paper proposes an interoperability improvement method using APCT combined with primary-side control principle. Firstly, adaptive operating mode switching is achieved so that the magnetic field can be switched and coupled with rectangular and DD coils. Secondly, inverter output currents detection is used to identify the type of receiving coils. Operating modes (SR mode and DD mode) are switched according to the identification result. Then, CC charging is achieved and the transmission efficiency is optimized with and without misalignment by employing mutual inductance estimation using only primary-side electrical information. Finally, the proposed method is validated by experiments. The experimental results show that maximum transmission efficiency can be maintained at 77% interoperating with rectangular and DD coils when coils are aligned or with an X offset and a Y offset of 50 mm. The proposed method is benefit to solving the problem that conventional transmitting coil cannot automatically interoperate with different receiving coils.

REFERENCES

- [1] Z. Dai, J. Wang, Y. Li, Y. He, Z. Fang, and H. Hou, "Optimal design of magnetic coupling wireless power supply system for monitoring equipment," *IEEE Access*, vol. 6, pp. 58600–58608, 2018.
- [2] C. C. Mi, G. Buja, S. Y. Choi, and C. T. Rim, "Modern advances in wireless power transfer systems for roadway powered electric vehicles," *IEEE Trans. Ind. Electron.*, vol. 63, no. 10, pp. 6533–6545, Oct. 2016.
- [3] C. Cai et al., "Design and optimization of load-independent magnetic resonant wireless charging system for electric vehicles," *IEEE Access*, vol. 6, pp. 17264–17274, 2018.
- [4] G. Ombach, D. Kurschner, S. Mathar, and W. Chlebosz, "Optimum magnetic solution for interoperable system for stationary wireless EV charging," in *Proc. 10th Int. Conf. Ecological Vehicles Renew. Energies (EVER)*, Mar./Apr. 2015, pp. 1–8.
- [5] W. Li, H. Zhao, T. Kan, and C. Mi, "Inter-operability considerations of the double-sided LCC compensated wireless charger for electric vehicle and plug-in hybrid electric vehicle applications," in *Proc. IEEE PELS Workshop Emerg. Technol., Wireless Power*, Jun. 2015, pp. 1–6.
- [6] G. Ombach, D. Kurschner, and S. Mathar, "Universal base coil solution for interoperable system for stationary wireless EV charging," in *Proc. Int. Conf. Sustain. Mobility Appl., Renew. Technol.*, Nov. 2015, pp. 1–9.
- [7] M. Budhia, J. T. Boys, G. A. Covic, and C.-Y. Huang, "Development of a single-sided flux magnetic coupler for electric vehicle IPT charging systems," *IEEE Trans. Ind. Electron.*, vol. 60, no. 1, pp. 318–328, Jan. 2013.
- [8] W. Zhang, J. C. White, A. M. Abraham, and C. C. Mi, "Loosely coupled transformer structure and interoperability study for EV wireless charging systems," *IEEE Trans. Power Electron.*, vol. 30, no. 11, pp. 6356–6367, Nov. 2015.
- [9] G. A. Covic, M. L. G. Kissin, D. Kacprzak, N. Clausen, and H. Hao, "A bipolar primary pad topology for EV stationary charging and highway power by inductive coupling," in *Proc. IEEE Energy Convers. Congr. Expo.*, Sep. 2011, pp. 1832–1838.
- [10] F. Y. Lin, S. Kim, G. A. Covic, and J. T. Boys, "Effective coupling factors for series and parallel tuned secondaries in IPT systems using bipolar primary pads," *IEEE Trans. Transport. Electrification*, vol. 3, no. 2, pp. 434–444, Jun. 2017.
- [11] Y. Liu, R. Mai, P. Yue, Y. Li, and Z. He, "Efficiency optimization for wireless dynamic charging system with overlapped DD coil arrays," in *Proc. IEEE Appl. Power Electron. Conf. Expo.*, Mar. 2017, pp. 1439–1442.
- [12] A. Zaheer, H. Hao, G. A. Covic, and D. Kacprzak, "Investigation of multiple decoupled coil primary pad topologies in lumped IPT systems for interoperable electric vehicle charging," *IEEE Trans. Power Electron.*, vol. 30, no. 4, pp. 1937–1955, Apr. 2015.
- [13] L. Xiang, X. Li, J. Tian, and Y. Tian, "A crossed DD geometry and its double-coil excitation method for electric vehicle dynamic wireless charging systems," *IEEE Access*, vol. 6, pp. 45120–45128, 2018.
- [14] P. Feng et al., "The modeling analysis of wireless power transmission under the basic topology structure," in *Proc. Int. Conf. Comput. Syst., Electron. Control*, Dec. 2017, pp. 362–367.
- [15] T. Thabet and J. Woods, "Impact of connection type on the efficiency of wireless power transfer systems," in *Proc. Int. Conf. Circuits, Syst. Simulation*, Jul. 2017, pp. 146–150.
- [16] W. Li, H. Zhao, S. Li, J. Deng, T. Kan, and C. Mi, "Integrated LCC compensation topology for wireless charger in electric and plug-in electric vehicles," *IEEE Trans. Ind. Electron.*, vol. 62, no. 7, pp. 4215–4225, Jul. 2015.
- [17] J. Deng, F. Lu, S. Li, T.-D. Nguyen, and C. Mi, "Development of a high efficiency primary side controlled 7kW wireless power charger," in *Proc. IEEE Int. Electr. Vehicle Conf.*, Dec. 2014, pp. 1–6.
- [18] W. Li, H. Zhao, J. Deng, S. Li, and C. C. Mi, "Comparison study on SS and double-sided LCC compensation topologies for EV/PHEV wireless chargers," *IEEE Trans. Veh. Technol.*, vol. 65, no. 6, pp. 4429–4439, Jun. 2016.
- [19] W. Zhang and C. C. Mi, "Compensation topologies of high-power wireless power transfer systems," *IEEE Trans. Veh. Technol.*, vol. 65, no. 6, pp. 4768–4778, Jun. 2016.
- [20] C. Wang, C. Zhu, K. Song, G. Wei, S. Dong, and R. G. Lu, "Primary-side control method in two-transmitter inductive wireless power transfer systems for dynamic wireless charging applications," in *Proc. IEEE PELS Workshop Emerg. Technol., Wireless Power Transf.*, May 2017, pp. 1–6.
- [21] Q. Zhu, Y. Guo, L. Wang, S. Li, and C. Liao, "Neighboring effects on the deactivated inverter in a segmented dynamic wireless EV charging system," in *Proc. Int. Power Electron. Conf.*, May 2018, pp. 3338–3343.
- [22] M. Ibrahim et al., "Inductive charger for electric vehicle: Advanced modeling and interoperability analysis," *IEEE Trans. Power Electron.*, vol. 31, no. 12, pp. 8096–8114, Dec. 2016.
- [23] Z. Li, C. Zhu, J. Jiang, K. Song, and G. Wei, "A 3-kW wireless power transfer system for sightseeing car supercapacitor charge," *IEEE Trans. Power Electron.*, vol. 32, no. 5, pp. 3301–3316, May 2017.
- [24] H. Li, Y. Liu, K. Zhou, Z. He, W. Li, and R. Mai, "Uniform power IPT system with three-phase transmitter and bipolar receiver for dynamic charging," *IEEE Trans. Power Electron.*, vol. 34, no. 3, pp. 2013–2017, Mar. 2019.
- [25] K. Hata, T. Imura, and Y. Hori, "Simultaneous estimation of primary voltage and mutual inductance based on secondary-side information in wireless power transfer systems," in *Proc. IEEE Wireless Power Transf. Conf.*, May 2016, pp. 1–3.
- [26] J. Yin, D. Lin, T. Parisini, and S. Y. Hui, "Front-end monitoring of the mutual inductance and load resistance in a series-series compensated wireless power transfer system," *IEEE Trans. Power Electron.*, vol. 31, no. 10, pp. 7339–7352, Oct. 2016.
- [27] J. P. W. Chow, H. S. H. Chung, and C. S. Cheng, "Online regulation of receiver-side power and estimation of mutual inductance in wireless inductive link based on transmitter-side electrical information," in *Proc. IEEE Appl. Power Electron. Conf. Expo.*, Mar. 2016, pp. 1795–1801.
- [28] Y.-G. Su, L. Chen, X.-Y. Wu, A. P. Hu, C.-S. Tang, and X. Dai, "Load and mutual inductance identification from the primary side of inductive power transfer system with parallel-tuned secondary power pickup," *IEEE Trans. Power Electron.*, vol. 33, no. 11, pp. 9952–9962, Nov. 2018.



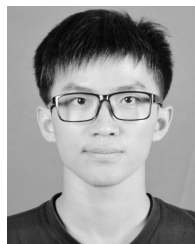
GUANG YANG received the B.S. degree from the School of Electrical and Information Engineering, Anhui University of Technology (AHUT), Ma'anshan, China, in 2014, and the M.S. degree from the School of Electrical Engineering and Automation, Harbin Institute of Technology (HIT), Harbin, China, in 2017, where he is currently pursuing the Ph.D. degree.

His research interest includes wireless charging technology for electric vehicles.



KAI SONG (M'12) received the B.S., M.S., and Ph.D. degrees in instrument science and technology from the Harbin Institute of Technology (HIT), Harbin, China, in 2005, 2007, and 2011, respectively.

In 2011, he joined the School of Electrical Engineering and Automation, HIT, as a Lecturer. From 2014 to 2015, he was a Visiting Scholar of electrical engineering with The University of Tokyo, Japan. Since 2016, he has been an Associate Professor with the School of Electrical Engineering and Automation, HIT. His current research interest includes wireless power transfer, particularly in the high-power wireless power transfer systems for electric vehicles and robots.



HANG ZHANG received the B.S. degree from the School of Control Science and Engineering, Shandong University (SDU), China, in 2018. He is currently pursuing the M.S. degree with the Harbin Institute of Technology (HIT), Harbin, China.

His research interest includes wireless power transfer.



RUIZHI WEI received the B.S. degree in information engineering for smart grid from the Nanjing University of Science and Technology (NJUST), Nanjing, China, in 2018. He is currently pursuing the M.S. degree in instrumentation engineering with the Harbin Institute of Technology (HIT), Harbin, China.

His research interests include contactless resonant converters and wireless power transfer systems.



QIAN ZHANG received the B.S. and M.S. degrees in electrical engineering from Beijing Jiaotong University (BJTU), Beijing, China, in 2012 and 2017, respectively.

She is currently an Assistant Engineer with the State Grid Beijing Power Research Institute. Her research interest includes wireless power transfer.



XIAOHUA HUANG received the B.S. degree from the School of Electrical Engineering, Shandong University (SDU), China, in 2002, and the Ph.D. degree in advanced technology of electrical engineering and energy from the Chinese Academy of Sciences (CAS), Beijing, China, in 2010.

She is currently a Senior Engineer with the China Electric Power Research Institute. Her research interest includes wireless power transfer.



CHUNBO ZHU (M'05) received the B.S. and M.S. degrees in electrical engineering and the Ph.D. degree in mechanical engineering from the Harbin Institute of Technology (HIT), Harbin, China, in 1987, 1992, and 2001, respectively.

He was a Postdoctoral Research Fellow with the PEI Research Center, National University of Ireland, Galway, Ireland, from 2003 to 2004. He has been a Lecturer with the Department of Automation Measurement and Control, HIT, since 1987. He is currently a Full Professor with HIT, where he leads the Laboratory of Wireless Power Transfer and Battery Management Technologies. His current research interests include energy management systems, electric and hybrid electric vehicles, and wireless power transfer technologies.

...